

1 **High-content imaging to phenotype antimicrobial effects on individual bacteria at scale**

2

3 Sushmita Sridhar<sup>1,2¶</sup>, Sally Forrest<sup>1¶</sup>, Benjamin Warne<sup>1</sup>, Mailis Maes<sup>1</sup>, Stephen Baker<sup>1</sup>,

4 Gordon Dougan<sup>1\*</sup>, Josefin Bartholdson Scott<sup>1\*</sup>

5

6 <sup>1</sup>Cambridge Institute of Therapeutic Immunology & Infectious Disease, University of

7 Cambridge Department of Medicine, Jeffrey Cheah Biomedical Centre, Puddicombe Way,

8 Cambridge Biomedical Campus, Cambridge CB2 0AW, United Kingdom

9 <sup>2</sup>Wellcome Sanger Institute, Hinxton, CB10 1SA, United Kingdom

10

11 <sup>¶</sup>These authors contributed equally

12

13 \*Corresponding authors: e-mail: [jb2143@cam.ac.uk](mailto:jb2143@cam.ac.uk) & [gd312@medschl.cam.ac.uk](mailto:gd312@medschl.cam.ac.uk)

14

15

16

17

18

19

20

21

22

23

24

25

26 **Abstract**

27 High-content imaging (HCI) is technique for screening multiple cells in high resolution to  
28 detect subtle morphological and phenotypic variation. The method has been commonly  
29 deployed on model eukaryotic cellular systems, often for screening new drugs and targets.  
30 HCI is not commonly utilised for studying bacterial populations but may be powerful tool in  
31 understanding and combatting antimicrobial resistance. Consequently, we developed a high-  
32 throughput method for phenotyping bacteria under antimicrobial exposure at the scale of  
33 individual bacterial cells. Imaging conditions were optimised on an Opera Phenix confocal  
34 microscope (Perkin Elmer) and novel analysis pipelines were established for both Gram-  
35 negative bacilli and Gram-positive cocci. The potential of this approach was illustrated using  
36 isolates of *Klebsiella pneumoniae*, *Salmonella enterica* serovar Typhimurium, and  
37 *Staphylococcus aureus*. HCI enabled the detection and assessment of subtle morphological  
38 characteristics, undetectable through conventional phenotypical methods, that could  
39 reproducibly distinguish between bacteria exposed to different classes of antimicrobials with  
40 distinct modes of action (MOA). In addition, distinctive responses were observed between  
41 susceptible and resistant isolates. By phenotyping single bacterial cells, we observed intra-  
42 population differences, which may be critical in identifying persistence or emerging  
43 resistance during antimicrobial treatment. The work presented here outlines a comprehensive  
44 method for investigating morphological changes at scale in bacterial populations under  
45 specific perturbation.

46

47 **Importance**

48 High-content imaging (HCI) is a microscopy technique that permits the screening of multiple  
49 cells simultaneously in high resolution to detect subtle morphological and phenotypic  
50 variation. The power of this methodology is that is can generate large datasets comprised of

51 multiple parameters taken from individual cells subjected to range of different conditions. We  
52 aimed to develop novel methods for using HCI to study bacterial cells exposed to a range of  
53 different antibiotic classes. Using an Opera Phenix confocal microscope (Perkin Elmer) and  
54 novel analysis pipelines we created a method to study the morphological characteristics of  
55 *Klebsiella pneumoniae*, *Salmonella enterica* serovar Typhimurium, and *Staphylococcus*  
56 *aureus* when exposed to antibacterial drugs with differing modes of action. By imaging  
57 individual bacterial cells at high resolution and scale, we observed intra-population  
58 differences associated with different antibiotics. The outlined methods are highly relevant for  
59 how we begin to better understand and combat antimicrobial resistance.

60

61 **Keywords**

62 High-content imaging, image analysis, bacteria, antimicrobial resistance, phenotyping

63

64

65

66

67

68

69

70

71

72

73

74

75

## 76 **Introduction**

77 Antimicrobial resistance (AMR) is one of the greatest current challenges in human health,  
78 with rising cases of antimicrobial resistant bacterial infections and a lack of new classes of  
79 licensed antimicrobials. Advances in bacterial genomics have revolutionised our ability to  
80 genotype antimicrobial resistant bacterial isolates at scale. However, it remains critical to link  
81 genotype with phenotype in order to interpret the biological and clinical relevance of AMR.  
82 Some phenotyping methods have been adapted to work at scale (e.g. antimicrobial  
83 susceptibility testing using semi-automated platforms such as the bioMérieux VITEK  
84 system), yet many others either rely on low throughput methods or aggregate data from  
85 mixed populations of bacterial cells. The analysis of bulk bacterial populations rather than  
86 individual cells potentially overlooks persister cells or the emergence of resistant or tolerant  
87 bacteria within that population. High throughput imaging of bacterial populations at the scale  
88 of individual cells has received limited attention but may be achieved by exploiting high-  
89 content microscopy.

90  
91 High-content imaging (HCI) can be utilised as a powerful phenotypic screening approach that  
92 combines automated microscopy with image analysis to quantify multiple morphological  
93 features. This approach may capture subtle differences in structure and shape not discernible  
94 by the human eye or conventional phenotypic methods. Such image-based profiling has great  
95 potential in high-throughput drug screening, which has mainly been applied to eukaryotic  
96 cells and tissue(1, 2). In the field of microbiology, HCI has predominantly been used to study  
97 intracellular pathogens such as *Mycobacterium tuberculosis*(3–6) and *Salmonella* species as  
98 they interact with host cells(7), but only recently to screen individual bacteria growing as a  
99 population in batch culture(8, 9). Pogliano and colleagues developed a bacterial cytological  
100 profiling assay to identify morphological changes in *Escherichia coli* and other species in



101 response to different classes of antimicrobials using fluorescence microscopy(10–13).  
102 Analysis of image data enabled the assignment of distinct morphological profiles correlating  
103 with the mechanism of action of the antimicrobial compounds tested(10). This method  
104 opened up a novel way of screening new therapeutic compounds simultaneously for efficacy  
105 and mode-of-action (MOA) using bacterial imaging(8–13).

106

107 Given the variety of AMR mechanisms harboured by bacterial species and, in many cases, by  
108 isolates of the same species, it is important to optimise HCI approaches for a range of  
109 bacteria. In this study, we developed and optimised a high-throughput imaging method based  
110 on HCI to systematically screen individual bacteria from three different species grown under  
111 antimicrobial exposure. We optimised bacterial imaging conditions using an Opera Phenix  
112 confocal microscope (Perkin Elmer) and established novel analysis pipelines for image  
113 segmentation and bacterial morphological analysis for both Gram-negative bacilli and Gram-  
114 positive cocci. The combination of HCI and image analysis enabled the detection of subtle  
115 morphological characteristics that differed between different antimicrobial classes. This work  
116 contributes to the expansion of microbial phenotyping from population-level to single-cell  
117 analysis and provides a comprehensive method of bacterial phenotypic screening at scale.

118

## 119 **Materials and Methods**

### 120 *Bacterial isolates*

121 A number of reference bacterial isolates, representing clinically important species, were  
122 analysed. This panel included one Gram-positive (*Staphylococcus aureus*) and two Gram-  
123 negative (*Salmonella enterica* serovar Typhimurium and *Klebsiella pneumoniae*) species.  
124 Two isolates were included per species, each with broadly different antimicrobial  
125 susceptibility profiles (Table 1).

126

127 *Antimicrobial susceptibility testing*

128 Antimicrobial susceptibility testing was performed for a range of clinically relevant  
129 antimicrobials with different MOAs (Table 1). Minimum Inhibitory Concentrations (MICs)  
130 were determined by ETESTs (bioMérieux) according to the manufacturer's instructions.  
131 Briefly, pure bacterial cultures were diluted in saline to 0.5 MacFarland standard, 100 µl of  
132 solution was inoculated and spread onto Isosensitest plates (Oxoid, CM0471), and an ETEST  
133 strip was placed on top. Plates were incubated for 16-18 hours at 37°C before the result was  
134 read.

135

136 *Preparation of plate coatings*

137 Coating matrices were prepared according to manufacturer recommendations in sterile  
138 conditions (Table S1). All coatings, except poly-L-lysine, were incubated in ultra-thin 96  
139 well plates (Perkin Elmer CellCarrier Ultra, 6655308) overnight at 37°C. The following day,  
140 wells were rinsed 1-3 times with wash buffer (Table S1). For poly-L-lysine, wells were  
141 coated for 5 minutes. The solution was aspirated, and wells were left to dry overnight at  
142 37°C.

143

144 *Bacterial imaging assay*

145 Overnight bacterial cultures were diluted in LB broth and mixed with antimicrobials to a final  
146 antimicrobial concentration of 5x MIC. Where an MIC could not be measured (i.e., where  
147 bacterial growth continued along the whole length of the ETEST), the upper limit of the  
148 ETEST was arbitrarily used in place of the MIC. The bacteria were incubated with and  
149 without antimicrobials in static incubators in ultra-thin 96 well plates for 2 hours at 37°C.  
150 The plates were aspirated, and the remaining adherent bacteria were fixed with 4%

151 paraformaldehyde (Alfa Aesar, J61899.AK) for 10 minutes. The wells were washed once  
152 with 50 $\mu$ l of DPBS (Thermo, 10010023) before staining. Fixed cells were stained with FM4-  
153 64 (2 $\mu$ g/ml, Thermo, T13320), SYTOX green (0.25 $\mu$ M, Thermo, S7020) and 4',6-  
154 Diamidino-2-phenylindole dihydrochloride (DAPI, 2 $\mu$ g/ml, Sigma, D9542). Staining was  
155 performed at ambient temperature for 20 minutes in the dark followed by a wash with 50 $\mu$ l  
156 PBS. Finally, 50 $\mu$ l of PBS was added to wells and the plates were imaged within 24 hours.

157

### 158 *High-content imaging and image analysis*

159 High-content confocal imaging was performed using an Opera Phenix (Perkin Elmer), using  
160 a 63x water immersion lens. 10 fields of view (equating to 0.4 mm<sup>2</sup>) were imaged for each  
161 well, with 3 z-stacks per field at 0.5  $\mu$ m intervals to ensure comprehensive imaging of the  
162 bacterial monolayer. Triplicate biological and technical replicates were performed for all  
163 experiments. Image analysis was performed using Harmony (v4.9). Optical correction was  
164 performed using flatfield and brightfield correction. The detailed full analysis pipelines are  
165 shown in Table S1 and S2. Data were exported and plotted in GraphPad Prism and R(14).

166

## 167 **Results**

### 168 *High-content imaging and analysis of individual bacteria*

169 An HCI workflow was established using two reference isolates from each of the three  
170 bacterial pathogens *S. Typhimurium*, *K. pneumoniae*, and *S. aureus* (Figure 1A; Table 1).  
171 Organisms were selected to have contrasting AMR profiles within each species. Each of the  
172 isolates was exposed to different antimicrobial agents, and HCI was used to collect  
173 phenotypic data for numerous individual bacteria within each assay. To this end, overnight  
174 bacterial cultures were grown in 96-well microtiter plates in the presence or absence of each  
175 antimicrobial for two hours to capture multiple early morphological changes. The

176 antimicrobials used are listed in Table 1. To capture images, the bacteria in each well were  
177 stained *in situ* with markers for the cell membrane (FM4-64), nucleic acid (DAPI), and  
178 membrane permeability (SYTOX green)(10) (Figure 1B). Imaging was performed on an  
179 Opera Phenix and image analysis was conducted using Harmony software.

180

181 As both rod- and cocci-shaped bacteria were imaged at the single cell scale, it was necessary  
182 to build separate, parallel pipelines for accurate analysis of microorganisms with different  
183 morphology. Examples of image segmentation and analysis of Gram-negative rods and  
184 Gram-positive cocci are shown in Figure 2 and detailed in Table S2 and Table S3,  
185 respectively. Images of Gram-negative rods were initially filtered using FM4-64 intensity  
186 patterns to enhance stained objects and subtract the background (Figure 2A). All images were  
187 then calculated based on DAPI and FM4-64 intensity and resized to include both cytosolic  
188 (DNA) and membrane regions; filtering was performed to remove artefacts such as  
189 incomplete bacterial bodies (Figure 2A and C). Morphological features and stain intensities  
190 were calculated for each defined bacterial cell, including area, roundness, width and length,  
191 as well as various measures of the intensity, symmetry and distribution of each of the FM4-  
192 64, DAPI and SYTOX green channels within each object (Figure 2B and D). For Gram-  
193 negative rods, the segmented objects were further classified as either single bacterial cells,  
194 dividing cells, or artefacts (Figure 2B) with a manually trained linear classifier using  
195 Harmony PhenoLOGIC. Subsequent analyses were conducted on the single cells only. The  
196 number of individual bacteria captured and analysed per well was dependent on isolate and  
197 treatment but was a minimum of 2,000 bacteria per untreated well for all replicates.

198

199 *Optimising bacterial imaging*

200 The bacterial isolates displayed different degrees of adhesion to the base of the 96-well  
201 plates, which significantly affected the image quality and downstream analysis. For example,  
202 the non-motile *K. pneumoniae* isolates spontaneously strongly adhered to the bottom of the  
203 wells, whereas the motile *S. Typhimurium* isolates displayed relatively poor adhesion  
204 resulting in blurry superimposed images of the flattened z-stack (maximum projection)  
205 (Figure S1A and B). Consequently, it was necessary to assess multiple plate coating  
206 conditions for each *S. Typhimurium* isolate to identify the optimal conditions for binding and  
207 image clarity. Ultimately, the image segmentation pipelines were used to quantify individual  
208 bacteria on 11 commercially available coating matrices (thick and thin rat tail collagen,  
209 Matrigel, vitronectin, fibronectin, Cell-Tak, laminin, wheat germ agglutinin (WGA), poly-L-  
210 lysine, gelatine, and mouse collagen) in comparison to non-coated wells (Table S1).

211  
212 The optimal coating conditions were found to differ between species, and to a lesser extent  
213 for each isolate (Figure 3). The *K. pneumoniae* isolates displayed the best adhesion and image  
214 quality on non-coated, WGA, and fibronectin-coated plates (Figure 3A, Figure S2A).

215 Therefore, all subsequent experiments with these isolates were conducted on non-coated  
216 wells. In contrast, image quality and the number of adherent *S. Typhimurium* bacteria  
217 improved dramatically upon optimization of the plate coating (Figure S1C). Both *S.*  
218 *Typhimurium* isolates displayed very poor adhesion to non-coated wells (Figure 3B; Figure  
219 S2B), but adhered sufficiently, although to different extents, to wells coated with thick rat tail  
220 collagen, Matrigel, and vitronectin (Figure 3B; Figure S2B), with collagen and vitronectin  
221 being the optimal conditions for NCTC 13347 and NCTC 13348 adhesion, respectively.

222 While different coatings were chosen for the two isolates, it would have been feasible to use  
223 the same coating, as the number and image quality of adhered organisms on rat tail collagen,  
224 Matrigel, and vitronectin were sufficient for analysis. To overcome any residual lack of

225 adhesion of *S. Typhimurium*, image analysis of these isolates was performed on individual  
226 planes rather than a maximum projection of three z-stacks.

227

228 The two *S. aureus* isolates displayed different adhesion properties, with ATCC 29213  
229 showing increased adhesion on vitronectin, fibronectin, Cell-Tak, WGA, and gelatin-coated  
230 wells, whereas NCTC 6571 only had sufficient cell counts on thin collagen and fibronectin  
231 coated wells (Figure 3C). Taking adhesion and image clarity (Figure S2C) into account, thin  
232 collagen and vitronectin were used for optimal adhesion of NCTC 6571 and NCTC 29213,  
233 respectively.

234

235 *Measuring distinct morphological changes in response to antimicrobial compounds*

236 To measure the phenotypic effects of antimicrobials with distinct mechanisms of action  
237 (MOAs), bacteria were incubated with 11 commercially available antimicrobials for 2 hours  
238 and imaged as described above. Antimicrobials were used at 5x the MIC determined by  
239 ETEST, or 5x the highest concentration tested if an isolate had an MIC higher than the  
240 ETEST range (Table 1). Figure 4A, 5A, and 6A show examples of the observed  
241 morphological changes at 2h post-treatment for a non-motile (*K. pneumoniae* NCTC 43816)  
242 and a motile Gram-negative rod (*S. Typhimurium* NCTC 13348), and a Gram-positive coccus  
243 (*S. aureus* ATCC 29213), respectively.

244

245 There were notable differences that the pipeline was able to capture between the effects of the  
246 same antimicrobials on Gram-negative versus Gram-positive bacteria, with more visually  
247 striking morphological changes observed in the Gram-negative bacteria. The established  
248 image analysis pipelines produced mean and standard deviation measurements for >90  
249 morphological features and stain intensities for each bacterium imaged (Table S4-6). These

250 measurements were combined for each isolate and analysed using principal component  
251 analysis (PCA). Technical replicates of each class of antimicrobial separated into distinct  
252 clusters based on MOA (Figure 4B, 5B and 6B, Figure S3), and biological replicates  
253 produced similar distribution by PCA, demonstrating assay reproducibility (Figure S4).  
254 Although separate pipelines were required for Gram-positive and Gram-negative organisms,  
255 each pipeline was able to distinguish a wide variety of phenotypes generated by antimicrobial  
256 treatment, segmenting the images and identifying individual bacteria despite the  
257 morphological changes associated with each antimicrobial (Figure S5).

258  
259 Antimicrobials acting on similar cellular processes generally induced comparable  
260 morphological changes in each species, and these were found to cluster in a PCA. Bacteria  
261 treated with tigecycline and gentamicin, which block protein synthesis by binding the 30S  
262 ribosomal subunit, clustered proximally for all Gram-negative isolates tested (Figure 4B, 5B).  
263 In addition, these generally also clustered near rifampicin and azithromycin treated bacteria  
264 (Fig 4B, 5B); these antimicrobials affect protein synthesis by inhibiting RNA polymerase or  
265 translation by binding the 50S ribosomal subunit, respectively. Antimicrobials that inhibit  
266 DNA synthesis (trimethoprim/sulphamethoxazole), DNA replication (ciprofloxacin) and cell  
267 wall synthesis (ampicillin, cefuroxime and meropenem) tended to induce an elongated  
268 phenotype and again clustered proximally (Fig 4B, 5B). Notably, meropenem clustered  
269 separately to the other  $\beta$ -lactams for the *Klebsiella* isolates and appeared to disrupt the  
270 bacterial cell wall more potently, causing the bacteria to swell and lyse instead of elongating  
271 (Figure 4, S3A). *K. pneumonia* NCTC 13438 was resistant to ampicillin,  
272 trimethoprim/sulphamethoxazole, cefuroxime and ciprofloxacin at concentrations higher than  
273 the ETEST scale, and with the exception of ciprofloxacin, these clustered with the untreated  
274 control (Figure S3A). A similar phenotype was observed for *S. Typhimurium* NCTC 13348

275 treated with ampicillin (Figure 5B). This highlights that HCI screens provide novel data  
276 regarding drug susceptibility as well as MOA.

277

278 The morphological changes observed for *S. aureus* were relatively subtle compared to those  
279 for the Gram-negative isolates (Figure 6A). Only ciprofloxacin induced a visually discernible  
280 phenotypic change, which was associated with enlarging bacterial area. However, after image  
281 analysis, each antimicrobial effectively separated into unique clusters by PCA, except  
282 trimethoprim/sulphamethoxazole, which clustered alongside the untreated controls. (Figure  
283 6B, S3C, S5). This finding suggests that the analysis could discriminate between very subtle  
284 cellular variation by capturing and analysing a large number of phenotypic parameters.

285

286 *Measuring the relative importance of specific morphological and fluorescence intensity*  
287 *parameters*

288 To assess the quality of the image analysis we calculated the Z prime (Z') values using  
289 Harmony, comparing treated and untreated bacteria for each species and antimicrobial  
290 combinations (Table S7-9), where an ideal assay should yield values between 0.5 and 1(15).  
291 The Z' values were higher for antimicrobials that clustered further from the untreated control  
292 in the PCA, and the Gram-negative isolates generally had more Z' values above 0.5 than the  
293 Gram-positive isolates. For example, the trimethoprim/sulphamethoxazole-treated *S. aureus*  
294 ATCC 29213 failed to separate from the untreated control by PCA, which correlated with  
295 poor Z' values (Table S9). Similarly, poor Z' values were obtained for azithromycin-treated  
296 *K. pneumoniae* NCTC 43816 (which is intrinsically resistant to macrolides) and gentamicin-  
297 treated *S. Typhimurium* NCTC 13348 (Table S7-8).

298



299 To highlight the relative importance of some of the measured parameters with high Z' values,  
300 differences in measurements across representative antimicrobials were compared.

301 Morphological measurements of roundness, area and length-to-width ratio (Figure 7), as well  
302 as threshold compactness and the radial relative deviation of the DAPI and FM4-64 staining  
303 patterns, were plotted for a selection of antimicrobials with different MOAs (Figure S6). In  
304 addition, SYTOX green intensity was included as this should only stain bacteria if membrane  
305 integrity has been compromised (Figure S6 M-O).

306

307 When plotting these parameters individually, clear differences were observed between the  
308 different antimicrobials for the *K. pneumoniae* isolates and, to a lesser extent, the *S.*  
309 *Typhimurium* isolates. For example, increased area, decreased roundness, increased length-to-  
310 -width ratio and FM4-64 and DAPI radial relative deviation correlated with the observed  
311 elongation phenotype observed for cefuroxime and ciprofloxacin (Figure 7 A, B, D, E, G, H  
312 and Figure S6 A, B, D, E). In contrast, increased FM4-64 and DAPI threshold compactness  
313 as well as bacterial roundness was observed for rifampicin and tigecycline (Figure 7 D, E,  
314 and Figure S6 G, H, J, K).

315

316 Generally, SYTOX green intensity was higher for antimicrobials disrupting the bacterial  
317 membrane for both Gram-negative (meropenem) and Gram-positive isolates (oxacillin).  
318 However, the effect of individual parameters on *S. aureus* were subtler than for the Gram-  
319 negative isolates, with only gentamicin treatment showing slightly decreased roundness and  
320 increased length-to width ratio (Figure 7 F and I), demonstrating the need to observe multiple  
321 combined phenotypic parameters.

322

323 *Phenotypes within a bacterial population*

324 Using violin plots, it was possible to visualize the population density and distribution of  
325 bacteria for any given parameter. This analysis demonstrated the inherent morphological  
326 heterogeneity in bacterial populations of the same isolate under the same growth conditions  
327 (Figure 7 and S6). For example, certain antimicrobial treatments yielded a high degree of  
328 heterogeneity in the length-to-width ratio, notably cefuroxime and ciprofloxacin treated *K.*  
329 *pneumoniae* NTCT 43816 (Figure 8). In contrast, rifampicin treatment appeared to yield  
330 decreased variability within a population as compared to untreated controls (Figure 8). By  
331 phenotyping single cells, it is possible to observe within-population differences, which is  
332 critical for identifying persistence or emerging resistance during antimicrobial treatment.

333

## 334 **Discussion**

335 In this study we optimised an experimental pipeline for high-throughput confocal imaging of  
336 motile and non-motile bacteria in liquid culture. We used this method for systematic  
337 screening of Gram-positive and Gram-negative bacteria under antimicrobial pressure, with  
338 robust and standardised image analysis pipelines to efficiently and reproducibly measure  
339 distinct morphological changes correlating with antimicrobial MOA. This analysis was built  
340 around profiling the subtle morphological phenotypes of individual bacteria in a culture,  
341 providing information on the whole population and variation within that population.

342

343 There is a number of advantages to using HCI for bacterial research. It provides flexibility in  
344 experimental design, with the ability to customise and compare growth conditions and  
345 individual isolates from different species in high throughput. Traditional phenotyping  
346 methods rely on the collective properties of large numbers of bacteria, HCI enables  
347 measurements at the scale of individual bacterial cells. Advances in image analysis permit  
348 reliable segmentation of bacterial images and rapid, detailed profiling of individual bacterial

349 cells with the ability to demonstrate the heterogeneity of bacterial phenotypes in any given  
350 environment.

351

352 Our work identified some challenges in using HCI for bacterial research, in particular  
353 variation in adhesion to microtiter plates. Poor adhesion influences both image quality and  
354 the number of bacteria successfully imaged for downstream analysis. This challenge was  
355 overcome by testing a range of coating matrices, which demonstrated substantial inter- and  
356 some intra-species variation in their ability to adhere to each substrate. For example, there  
357 were notable differences in adhesion between the non-motile *K. pneumoniae* and motile *S.*  
358 *Typhimurium*. *K. pneumoniae* possess an array of adhesins that allow them to adhere and  
359 persist in different environments, which have contributed to their emergence as an important  
360 nosocomial pathogen(16, 17). In contrast, *S. Typhimurium* relies on motility and more  
361 specific cellular interactions and invasion for causing infection(7). These factors highlight the  
362 need to optimise imaging conditions for each bacterial isolate. However, for most isolates,  
363 more than one coating condition was sufficient for downstream analysis, making it possible  
364 to screen multiple isolates in parallel using the same plate coating for the higher throughput  
365 assays.

366

367 One of the most challenging aspects of image analysis was the segmentation and  
368 identification of individual bacteria. This is in part because most existing image analysis  
369 software is designed primarily to analyse images of eukaryotic cells. However, analysis  
370 pipelines to effectively segment both rod- and cocci-shaped bacteria were created using  
371 existing image analysis tools in the Harmony software. Though the analysis pipelines in this  
372 study were created using Harmony, which is a proprietary software from Perkin Elmer, there

373 are open access image analysis software options available - for example CellProfiler(18) and  
374 Cellpose(19)– which have similar analysis capabilities.

375

376 It was necessary to produce separate pipelines for cocci and rod-shaped bacteria for the initial  
377 segmentation. Other studies have also utilised different pipelines for phenotypically variant  
378 species; for example, the analysis used by Zoffmann and colleagues for *E. coli* was not  
379 suitable for *Acinetobacter baumannii*, as these species differ in size and shape(8).

380 Importantly, the pipelines created in our study could be used to reproducibly segment bacteria  
381 in all growth conditions used, even as morphologies changed due to antimicrobial exposure.

382 Distinct morphological changes were observed in response to different classes of  
383 antimicrobials, with different effects observed in Gram-negative versus Gram-positive  
384 species. However, bacteria from the same species generally displayed similar morphological  
385 distributions by principal component analysis when treated with 5x the MIC, correlating with  
386 antimicrobial mechanism. In addition, different clustering was observed between susceptible  
387 and resistant isolates, allowing for simultaneous evaluation of potency as well as MOA.

388

389 The phenotypic changes identified in this study in the presence of antimicrobials are  
390 comparable to previous imaging studies in *Enterobacteriaceae*, including bacterial  
391 enlargement with carbapenems and cephalosporins(20, 21), compaction of the nucleoid with  
392 antimicrobials targeting the bacterial ribosome(22) and filamentous elongation in the  
393 presence of fluoroquinolones(23). In agreement with other studies, we identified similar  
394 morphological changes in isolates of *K. pneumoniae* and *S. Typhimurium* to those previously  
395 reported for *E. coli* in response to a range of antimicrobial classes(10), but here we employed  
396 a simplified method by removing centrifugation steps and by imaging directly in wells rather  
397 than on agarose pads. This facilitates higher throughput and scalability.

398

399 The fluorescent staining protocol previously optimised by Nonejuie *et al.*(10) worked well  
400 across all the isolates tested in this study. FM4-64 stains the cell membrane, and the staining  
401 patterns should relate to membrane integrity. DAPI and SYTOX green both stain nucleic  
402 acids, but only DAPI is permeable through an intact cell membrane, making SYTOX green  
403 intensity an additional measurement of membrane integrity after antimicrobial exposure(24,  
404 25). In addition, nucleic acid stains can distinguish between subtle alterations in nucleic acid  
405 distribution patterns. Plotting individual phenotypic parameters was sufficient when an  
406 antimicrobial induced a strong visual phenotypic effect, for example, length-to-width ratio  
407 could be used for ciprofloxacin or cefuroxime treated *K. pneumoniae*. However, in most  
408 cases, and in particular for the smaller cocci-shaped *S. aureus* isolates where the phenotypic  
409 effects were subtler, a combination of morphological as well as stain intensities, distribution  
410 and symmetry measurements were required to efficiently evaluate the data. This highlights  
411 that the software can detect important variations that are not obvious in conventional  
412 phenotypic methods.

413

414 Our methods contribute to moving microbial phenotyping from a population-based analysis  
415 to the scale of individual bacterial cells and provides a comprehensive method of bacterial  
416 phenotypic screening at scale. This approach has a wide range of applications, but the ability  
417 to provide analysis of diverse collections of isolates simultaneously in a range of growth  
418 conditions gives it important potential in the fight against AMR. In addition to existing roles  
419 in compound screening for antimicrobial efficacy and simultaneous MOA prediction(26), the  
420 technology could be used for more detailed mechanistic follow up studies using mutant  
421 libraries to assess genes that are protective against individual drugs(27). Large numbers of  
422 compounds and bacterial isolates, representing species with diverse genetic backgrounds, can

423 be screened at scale. We have previously shown the utility of bacterial HCI for therapeutic  
424 antibody screening(9), and there is potential to assess synergy between antimicrobials and  
425 monoclonal antibodies against multi-drug resistant bacteria that would be challenging using  
426 other platforms. Importantly, by analysing individual bacteria within a culture, it is possible  
427 to detect differential effects and persister cells during drug treatment and be able to truly  
428 evaluate the efficacy of a compound.

429

### 430 **Acknowledgments**

431 We thank James Hutt and Achim Kirsch for their help with the analysis pipelines. This work  
432 was supported by a Innovate UK Commercial in Confidence grant to purchase the Opera  
433 Phenix. SS and SB are funded by the Wellcome Trust (206194 and 215515/Z/19/Z). SF, BW,  
434 MM, SB, GD and SJB are supported by funding from the National Institute for Health  
435 Research [Cambridge Biomedical Research Centre at the Cambridge University Hospitals  
436 NHS Foundation Trust] and National Institute for Health Research AMR Research Capital  
437 Funding Scheme [NIHR200640]. The views expressed are those of the authors and not  
438 necessarily those of the NHS, the NIHR or the Department of Health and Social Care.

439

### 440 **Data Availability**

441 All data underlying the results are available in the supplementary files associated with the  
442 article.

443

### 444 **References**

- 445 1. van Vliet E, Daneshian M, Beilmann M, Davies A, Fava E, Fleck R, Julé Y, Kansy M,  
446 Kustermann S, Macko P, Mundy WR, Roth A, Shah I, Uteng M, van de Water B,  
447 Hartung T, Leist M. 2014. Current approaches and future role of high content imaging

- 448 in safety sciences and drug discovery. *ALTEX* 31:479–493.
- 449 2. Bray M-A, Singh S, Han H, Davis CT, Borgeson B, Hartland C, Kost-Alimova M,  
450 Gustafsdottir SM, Gibson CC, Carpenter AE. 2016. Cell Painting, a high-content  
451 image-based assay for morphological profiling using multiplexed fluorescent dyes. *Nat*  
452 *Protoc* 11:1757–1774.
- 453 3. Christophe T, Ewann F, Jeon HK, Cechetto J, Brodin P. 2010. High-content imaging  
454 of *Mycobacterium tuberculosis*-infected macrophages: an in vitro model for  
455 tuberculosis drug discovery. *Future Med Chem* 2:1283–1293.
- 456 4. Barczak AK, Avraham R, Singh S, Luo SS, Zhang WR, Bray MA, Hinman AE,  
457 Thompson M, Nietupski RM, Golas A, Montgomery P, Fitzgerald M, Smith RS,  
458 White DW, Tischler AD, Carpenter AE, Hung DT. 2017. Systematic, multiparametric  
459 analysis of *Mycobacterium tuberculosis* intracellular infection offers insight into  
460 coordinated virulence. *PLoS Pathog* 13:1–27.
- 461 5. Manning AJ, Ovechkina Y, McGillivray A, Flint L, Roberts DM, Parish T. 2017. A  
462 high content microscopy assay to determine drug activity against intracellular  
463 *Mycobacterium tuberculosis*. *Methods* 127:3–11.
- 464 6. Greenwood DJ, Dos Santos MS, Huang S, Russell MRG, Collinson LM, MacRae JI,  
465 West A, Jiang H, Gutierrez MG. 2019. Subcellular antibiotic visualization reveals a  
466 dynamic drug reservoir in infected macrophages. *Science (80- )* 364:1279–1282.
- 467 7. Antoniou AN, Powis SJ, Kriston-Vizi J. 2019. High-content screening image dataset  
468 and quantitative image analysis of *Salmonella* infected human cells. *BMC Res Notes*  
469 12:1–4.
- 470 8. Zoffmann S, Vercruysse M, Benmansour F, Maunz A, Wolf L, Blum Marti R, Heckel  
471 T, Ding H, Truong HH, Prummer M, Schmucki R, Mason CS, Bradley K, Jacob AI,  
472 Lerner C, Araujo del Rosario A, Burcin M, Amrein KE, Prunotto M. 2019. Machine

- 473 learning-powered antibiotics phenotypic drug discovery. *Sci Rep* 9:1–14.
- 474 9. Maes M, Dyson ZA, Smith SE, Goulding DA, Ludden C, Baker S, Kellam P, Reece  
475 ST, Dougan G, Scott JB. 2020. A novel therapeutic antibody screening method using  
476 bacterial high-content imaging reveals functional antibody binding phenotypes of  
477 *Escherichia coli* ST131. *bioRxiv* 2020.05.22.110148.
- 478 10. Nonejuie P, Burkart M, Pogliano K, Pogliano J. 2013. Bacterial cytological profiling  
479 rapidly identifies the cellular pathways targeted by antibacterial molecules. *Proc Natl*  
480 *Acad Sci* 110:16169–16174.
- 481 11. Quach DT, Sakoulas G, Nizet V, Pogliano J, Pogliano K. 2016. Bacterial Cytological  
482 Profiling (BCP) as a Rapid and Accurate Antimicrobial Susceptibility Testing Method  
483 for *Staphylococcus aureus*. *EBioMedicine* 4:95–103.
- 484 12. Lamsa A, Lopez-Garrido J, Quach D, Riley EP, Pogliano J, Pogliano K. 2016. Rapid  
485 Inhibition Profiling in *Bacillus subtilis* to Identify the Mechanism of Action of New  
486 Antimicrobials. *ACS Chem Biol* 11:2222–2231.
- 487 13. Htoo HH, Brumage L, Chaikeeratisak V, Tsunemoto H, Sugie J, Tribuddharat C,  
488 Pogliano J, Nonejuie P. 2019. Bacterial Cytological Profiling as a Tool To Study  
489 Mechanisms of Action of Antibiotics That Are Active against *Acinetobacter*  
490 *baumannii*. *Antimicrob Agents Chemother* 63:1–11.
- 491 14. Team RC. 2014. R: A language and environment for statistical computing. R Core  
492 Team (2014) R A Lang Environ Stat Comput R Found Stat Comput Vienna,  
493 Austria(available from <http://wwwR-project.org/>).
- 494 15. Zhang J-H, Chung TDY, Oldenburg KR. 1999. A Simple Statistical Parameter for Use  
495 in Evaluation and Validation of High Throughput Screening Assays. *J Biomol Screen*  
496 4:67–73.
- 497 16. Di Martino P, Cafferini N, Joly B, Darfeuille-Michaud A. 2003. *Klebsiella*



- 498 pneumoniae type 3 pili facilitate adherence and biofilm formation on abiotic surfaces.  
499 Res Microbiol 154:9–16.
- 500 17. Hassan MZ, Sturm-Ramirez K, Rahman MZ, Hossain K, Aleem MA, Bhuiyan MU,  
501 Islam MM, Rahman M, Gurley ES. 2019. Contamination of hospital surfaces with  
502 respiratory pathogens in Bangladesh. PLoS One 14:e0224065.
- 503 18. Carpenter AE, Jones TR, Lamprecht MR, Clarke C, Kang IH, Friman O, Guertin DA,  
504 Chang JH, Lindquist RA, Moffat J, Golland P, Sabatini DM. 2006. CellProfiler: image  
505 analysis software for identifying and quantifying cell phenotypes. Genome Biol  
506 7:R100.
- 507 19. Stringer C, Wang T, Michaelos M, Pachitariu M. 2020. Cellpose: a generalist  
508 algorithm for cellular segmentation. Nat Methods [https://doi.org/10.1038/s41592-020-](https://doi.org/10.1038/s41592-020-01018-x)  
509 01018-x.
- 510 20. Van Laar TA, Chen T, You T, Leung KP. 2015. Sublethal concentrations of  
511 carbapenems alter cell morphology and genomic expression of *Klebsiella pneumoniae*  
512 biofilms. Antimicrob Agents Chemother 59:1707–1717.
- 513 21. Horii T, Kobayashi M, Sato K, Ichiyama S, Ohta M. 1998. An in-vitro study of  
514 carbapenem-induced morphological changes and endotoxin release in clinical isolates  
515 of gram-negative bacilli. J Antimicrob Chemother 41:435–442.
- 516 22. Zimmerman SB. 2006. Shape and compaction of *Escherichia coli* nucleoids. J Struct  
517 Biol 156:255–261.
- 518 23. Zahller J, Stewart PS. 2002. Transmission electron microscopic study of antibiotic  
519 action on *Klebsiella pneumoniae* biofilm. Antimicrob Agents Chemother 46:2679–  
520 2683.
- 521 24. Roth BL, Poot M, Yue ST, Millard PJ. 1997. Bacterial viability and antibiotic  
522 susceptibility testing with SYTOX green nucleic acid stain. Appl Environ Microbiol

- 523 63:2421–2431.
- 524 25. McKenzie K, Maclean M, Grant MH, Ramakrishnan P, MacGregor SJ, Anderson JG.  
525 2016. The effects of 405 nm light on bacterial membrane integrity determined by salt  
526 and bile tolerance assays, leakage of UV-absorbing material and SYTOX green  
527 labelling. *Microbiol (United Kingdom)* 162:1680–1688.
- 528 26. Ang MLT, Pethe K. 2016. Contribution of high-content imaging technologies to the  
529 development of anti-infective drugs. *Cytom Part A* 89:755–760.
- 530 27. Zahir T, Camacho R, Vitale R, Ruckebusch C, Hofkens J, Fauvart M, Michiels J.  
531 2019. High-throughput time-resolved morphology screening in bacteria reveals  
532 phenotypic responses to antibiotics. *Commun Biol* 2:269.
- 533

534 **Figures and Tables**

535

536 **Table 1: Minimum Inhibitory Concentrations.**

| Species               | ID         | Ampicillin | Azithromycin | Trimethoprim-sulfamethoxazole | Ciprofloxacin | Gentamicin | Rifampicin | Meropenem | Tigecycline | Cefuroxime | Oxacillin | Vancomycin |
|-----------------------|------------|------------|--------------|-------------------------------|---------------|------------|------------|-----------|-------------|------------|-----------|------------|
| <i>K. pneumoniae</i>  | NCTC 13438 | >256*      | 32           | >32*                          | >32*          | 6          | 16         | 0.125     | 0.094       | >256*      | ND        | ND         |
| <i>K. pneumoniae</i>  | ATCC 43816 | 64         | 2            | 0.5                           | 0.16          | 1.5        | >32*       | 0.125     | 0.5         | 1.5        | ND        | ND         |
| <i>S. Typhimurium</i> | NCTC 13347 | 0.5        | 2            | 0.25                          | 0.012         | 2          | 16         | 0.125     | 0.19        | 3          | ND        | ND         |
| <i>S. Typhimurium</i> | NCTC 13348 | >256*      | 3            | 0.25                          | 0.012         | 3          | 24         | 0.064     | 0.19        | 3          | ND        | ND         |
| <i>S. aureus</i>      | NCTC 6571  | ND         | ND           | 0.125                         | 0.094         | 2          | ND         | ND        | ND          | ND         | 0.19      | 1          |
| <i>S. aureus</i>      | ATCC 29213 | ND         | ND           | 0.19                          | 0.25          | 2          | ND         | ND        | ND          | ND         | 0.38      | 1.5        |

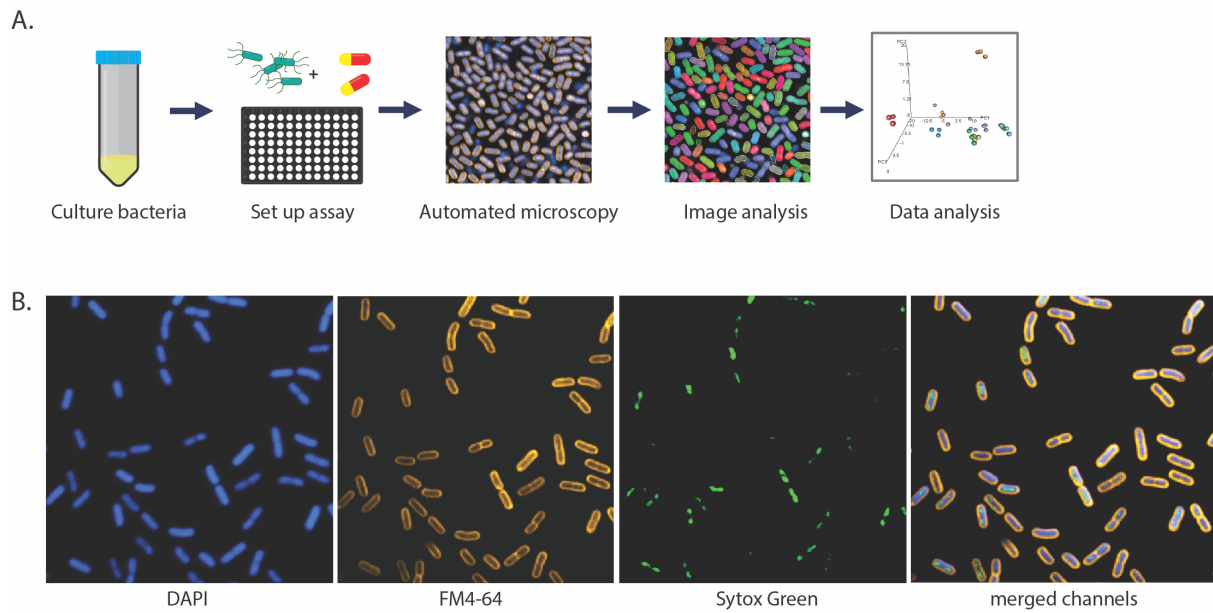
537

538 MICs were determined by ETEST and are presented in µg/ml. \* indicates the MIC is above the highest antimicrobial concentration on the

539 ETEST; ND indicates that MIC was not determined.

540

541



542

543

544 **Figure 1: Bacterial high-content imaging.** (A) Schematic of the bacterial high-content  
545 imaging workflow. Overnight bacterial cultures are added to ultra-thin bottom plates, and  
546 incubated, with or without antimicrobial compounds. Adherent bacteria are fixed and stained  
547 before being imaged on an Opera Phenix high-content confocal microscope using a 63x water  
548 immersion objective. Images were analysed using Harmony software and data was exported  
549 and plotted in R. (B) Representative image of *K. pneumoniae* NCTC 43816 stained with  
550 FM4-64 (cell membrane), DAPI (nucleic acid, membrane permeable) and SYTOX green  
551 (nucleic acid, membrane impermeable).

552

553

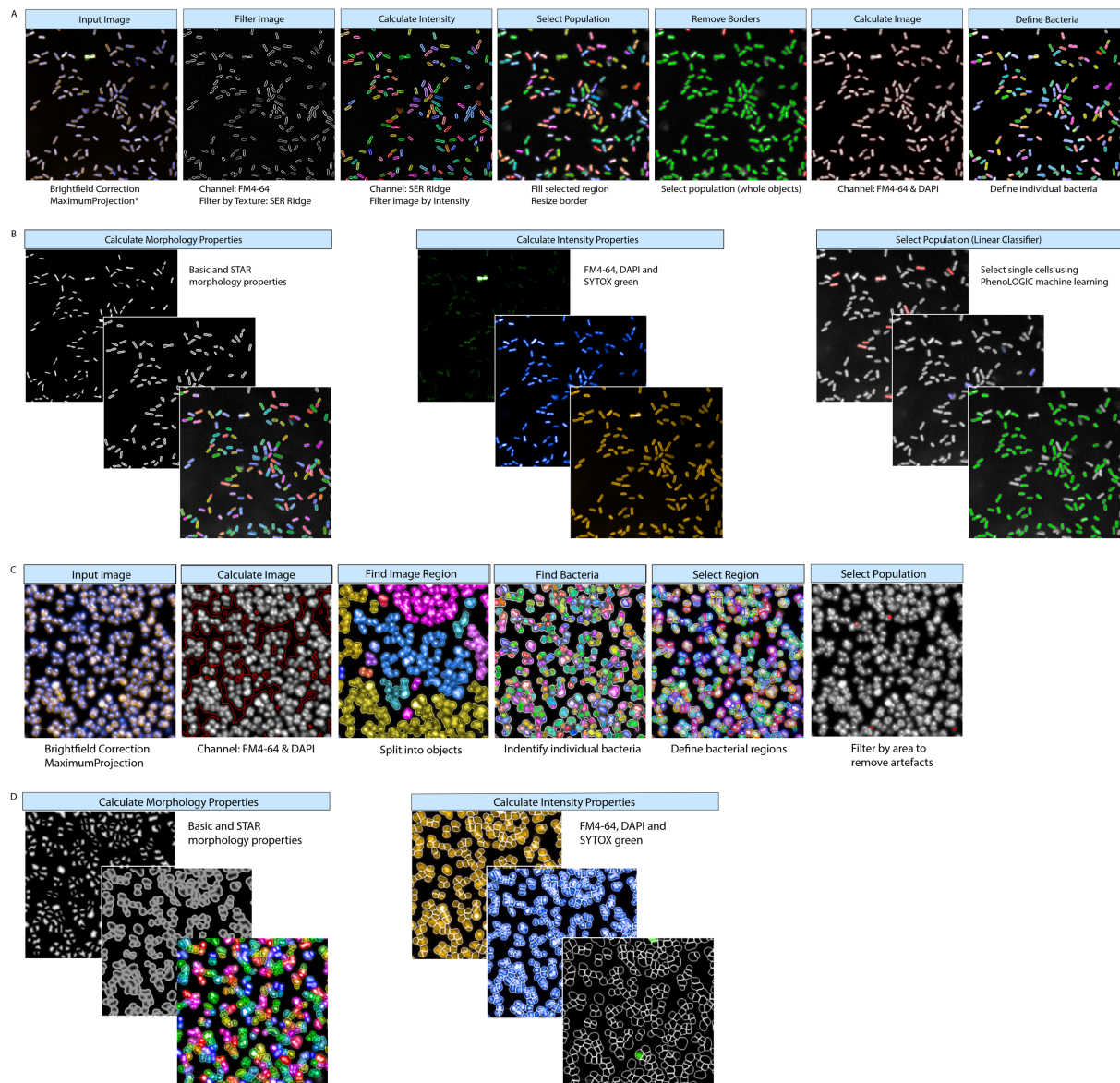
554

555

556

557

558



559

560 **Figure 2: Harmony bacterial image analysis workflow for Gram-negative rods (A-B)**

561 **and Gram-positive cocci (C-D).** (A) Using basic brightfield correction and maximum

562 projection, images were segmented by filtering the images using texture properties based on

563 the FM4-64 channel to remove any background. The image region was filled and resized and

564 border objects were excluded to include only whole objects. The image region was further

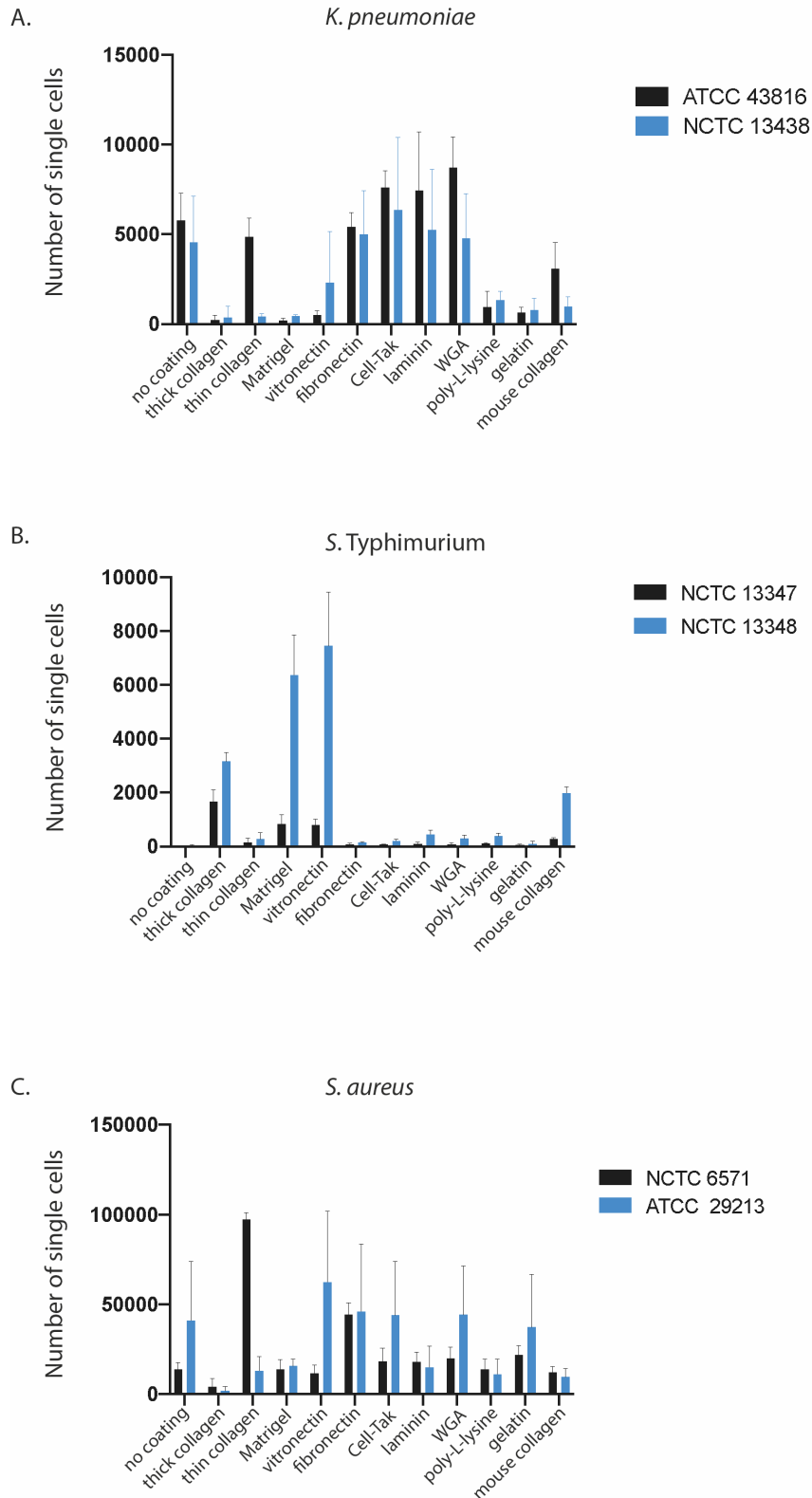
565 calculated using FM4-64 and DAPI fluorescence and individual bacteria were defined.

566 (\*single planes were analysed for *S. Typhimurium*) (B) Bacterial morphology and stain

567 intensity properties were calculated using DAPI, SYTOX Green and FM4-64 fluorescence.

568 Finally, a linear classifier was used to train the software to define single bacterial cells and

569 exclude any artefacts. **(C)** Using basic brightfield correction and maximum projection, the  
570 bacterial region was defined using a calculated image based on DAPI and FM4-64 channels.  
571 Individual bacteria were identified within the image region, and the bacterial regions were  
572 defined and resized into individual bacterial cells. Any artefacts were removed using size  
573 filters. **(D)** Bacterial morphology and stain intensity properties were calculated using DAPI,  
574 SYTOX Green and FM4-64 fluorescence.  
575



576

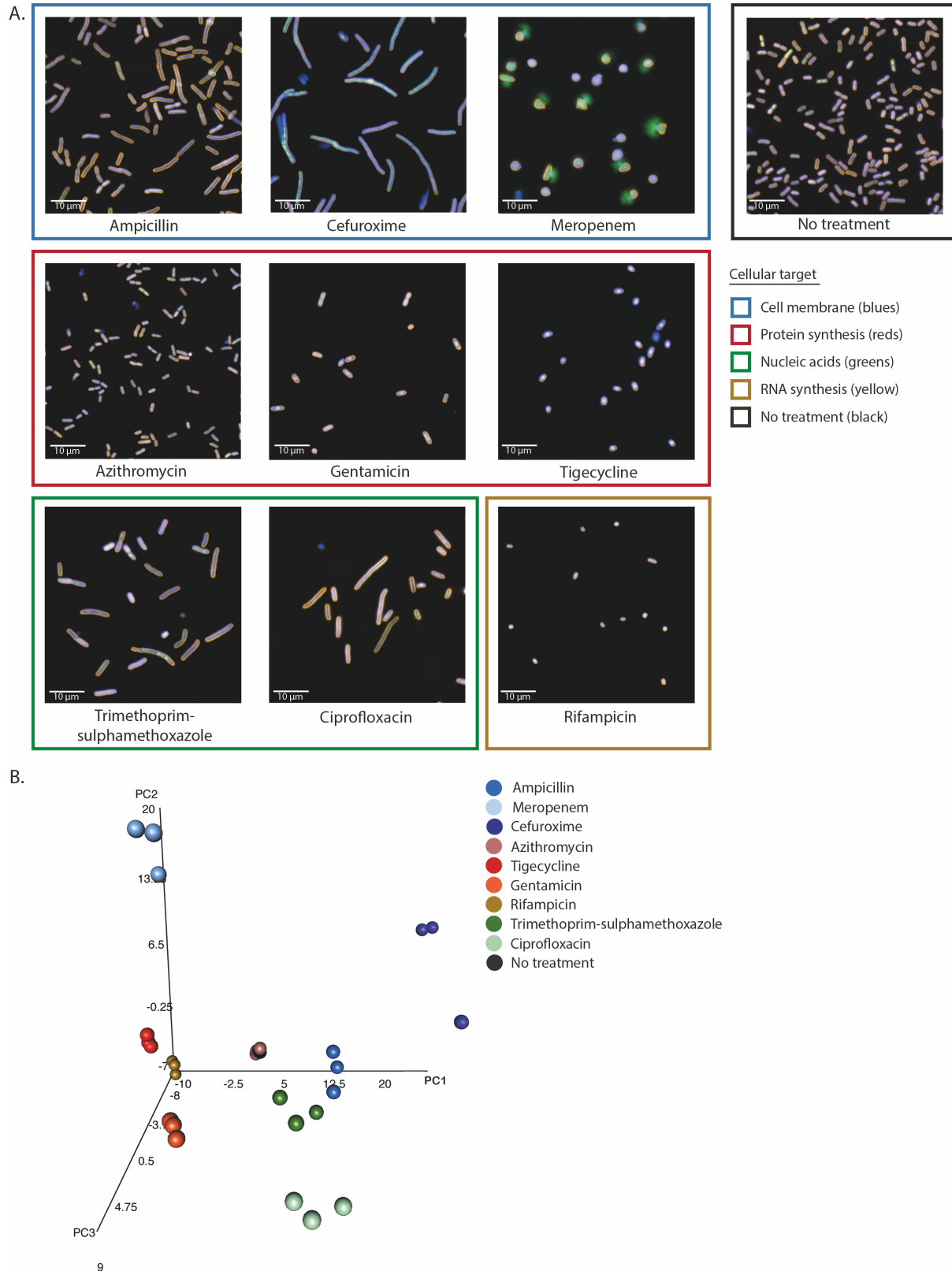
577 **Figure 3: Optimising plate coating for bacterial adhesion.** Isolates were grown in ultra-

578 thin 96 well plates on different surface matrices and the Harmony analysis pipelines were

579 used to count the number of adherent bacteria after fixing, washing and staining. Graphs are

580 comparing the adhesion of two representative isolates of *K. pneumoniae* (A), *S. Typhimurium*  
581 (B) and *S. aureus* (C) on each substrate. Error bars represent standard deviation of three  
582 biological replicates.  
583





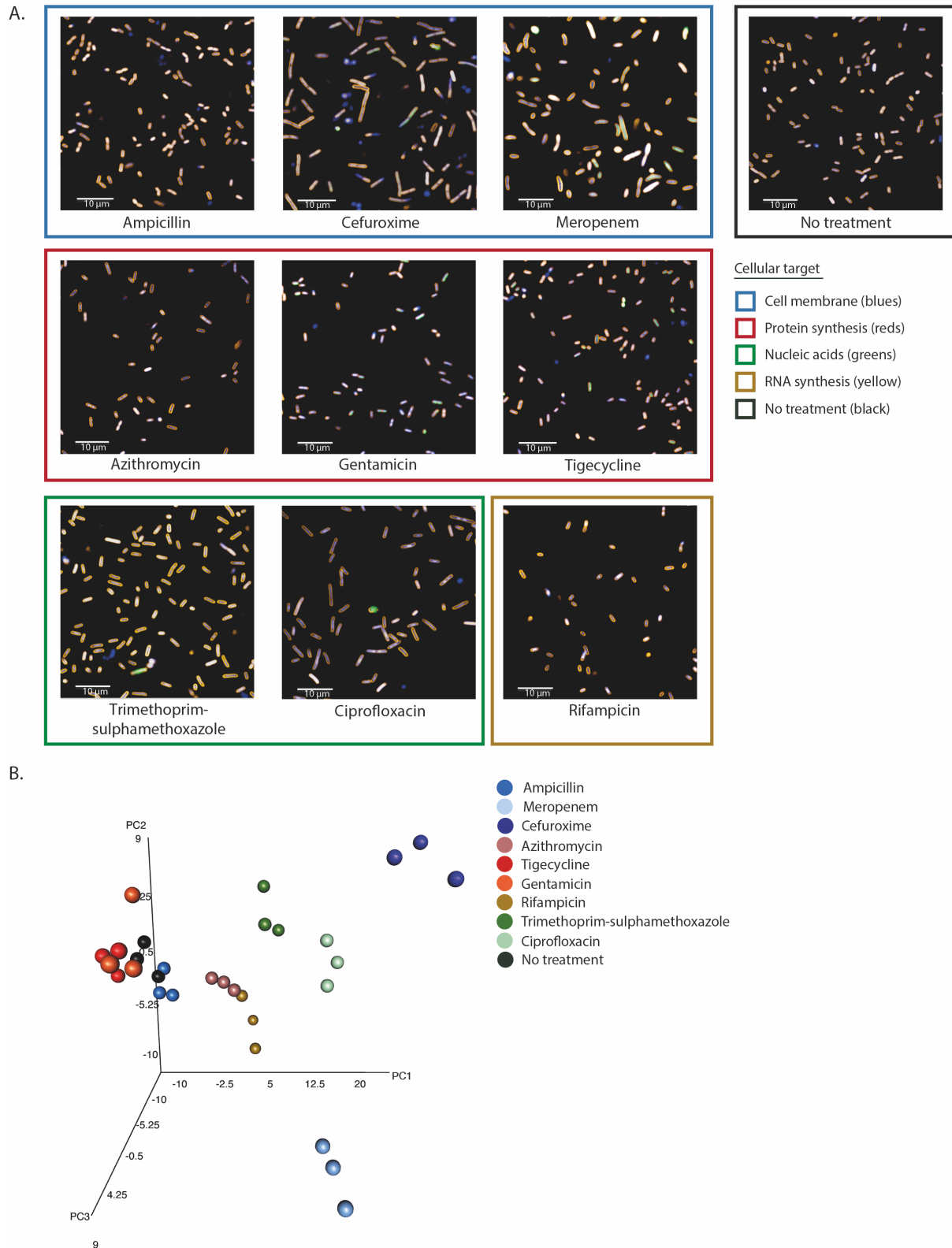
584

585 **Figure 4: Morphological effects on *K. pneumoniae* NCTC 43816 under antimicrobial**

586 **pressure. (A) Representative images of the effect of different antimicrobials on the *K.***

587 ***pneumoniae* isolate NCTC 43816 in exponential growth phase after 2 hours of incubation.**

588 Antimicrobials are grouped by similar cellular targets. Bacteria were stained with FM4-64,  
589 DAPI and SYTOX green. Images were acquired on an Opera Phenix using a 63x water  
590 immersion lens. **(B)** Three-dimensional principal component analysis of the mean and  
591 standard deviation values of 62 morphological properties measured for single bacterial cells  
592 in each well. Technical triplicate repeats are shown.



593

594 **Figure 5: Morphological effects on *S. Typhimurium* NCTC 13348 under antimicrobial**

595 **pressure. (A) Representative images of the effect of different antimicrobials on the *S.***

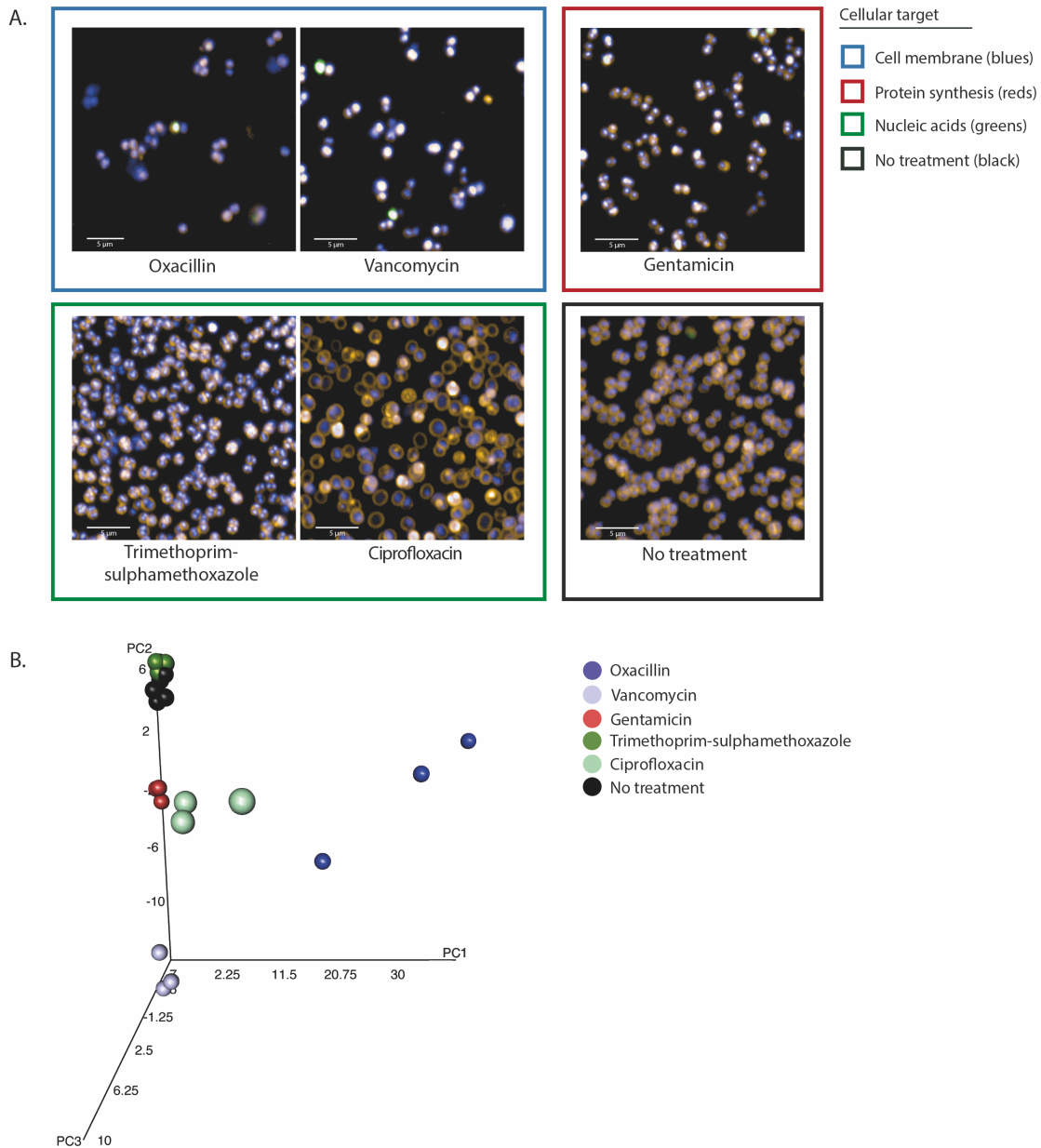
596 ***Typhimurium* isolate NCTC 13348 in exponential growth phase after 2 hours of incubation.**

597 Antimicrobials are grouped by similar cellular targets. Bacteria were stained with FM4-64,  
598 DAPI and SYTOX green. Images were acquired on an Opera Phenix using a 63x water  
599 immersion lens. **(B)** Three-dimensional principal component analysis of the mean and  
600 standard deviation values of 62 morphological properties measured for single bacterial cells  
601 in each well. Technical triplicate repeats are shown.

602

603

604



605

606 **Figure 6: Morphological effects on *S. aureus* ATCC 29213 under antimicrobial**

607 **pressure. (A)** Representative images of the effect of different antimicrobials on the *S. aureus*

608 isolate ATCC 29213 in exponential growth phase after 2 hours of incubation. Antimicrobials

609 are grouped by similar cellular targets. Bacteria were stained with FM4-64, DAPI and

610 SYTOX green. Images were acquired on an Opera Phenix using a 63x water immersion lens.

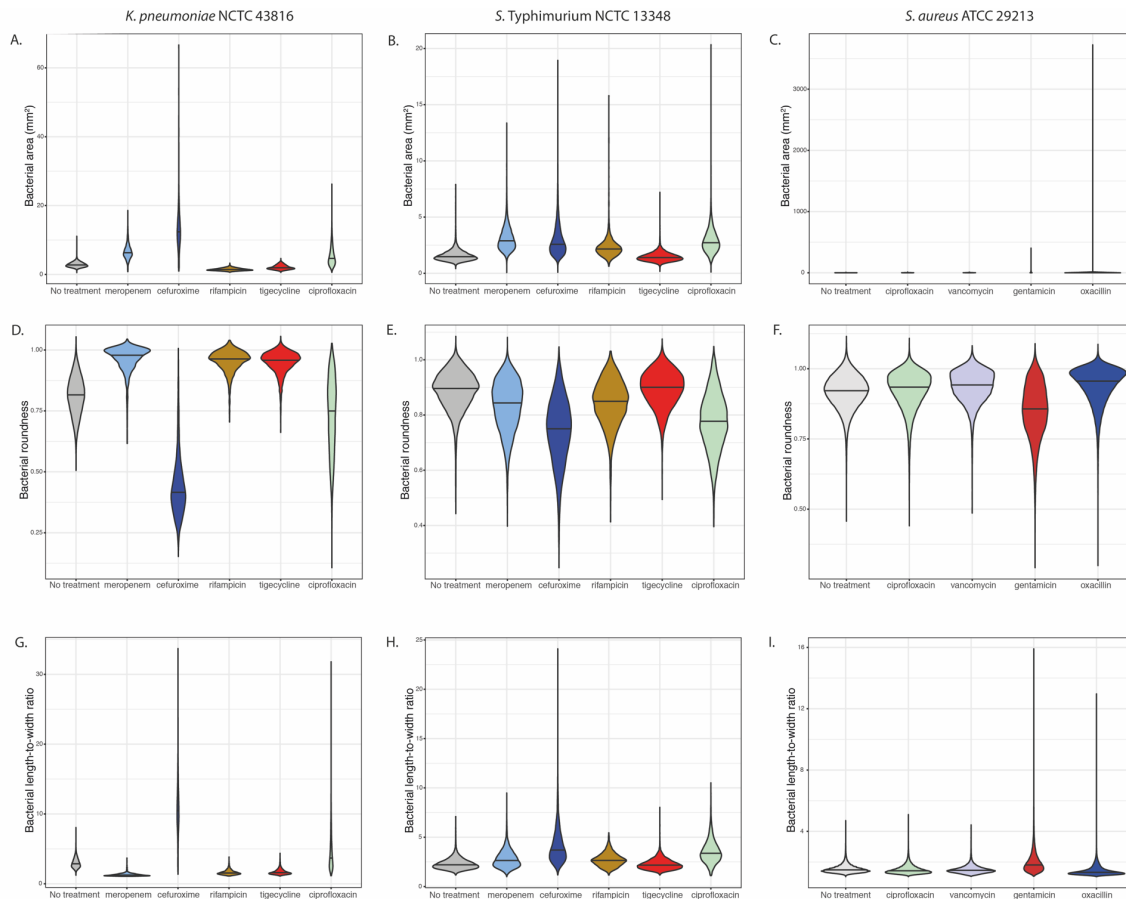
611 **(B)** Three-dimensional principal component analysis of the mean and standard deviation

612 values of 62 morphological properties measured for single bacterial cells in each well.

613 Technical triplicate repeats are shown.

614

615



616

617 **Figure 7: Comparison of individual basic morphological measurements.** Violin plots of

618 bacterial area (A-C), bacterial roundness (D-F) and bacterial length-to-width ratio (G-I)

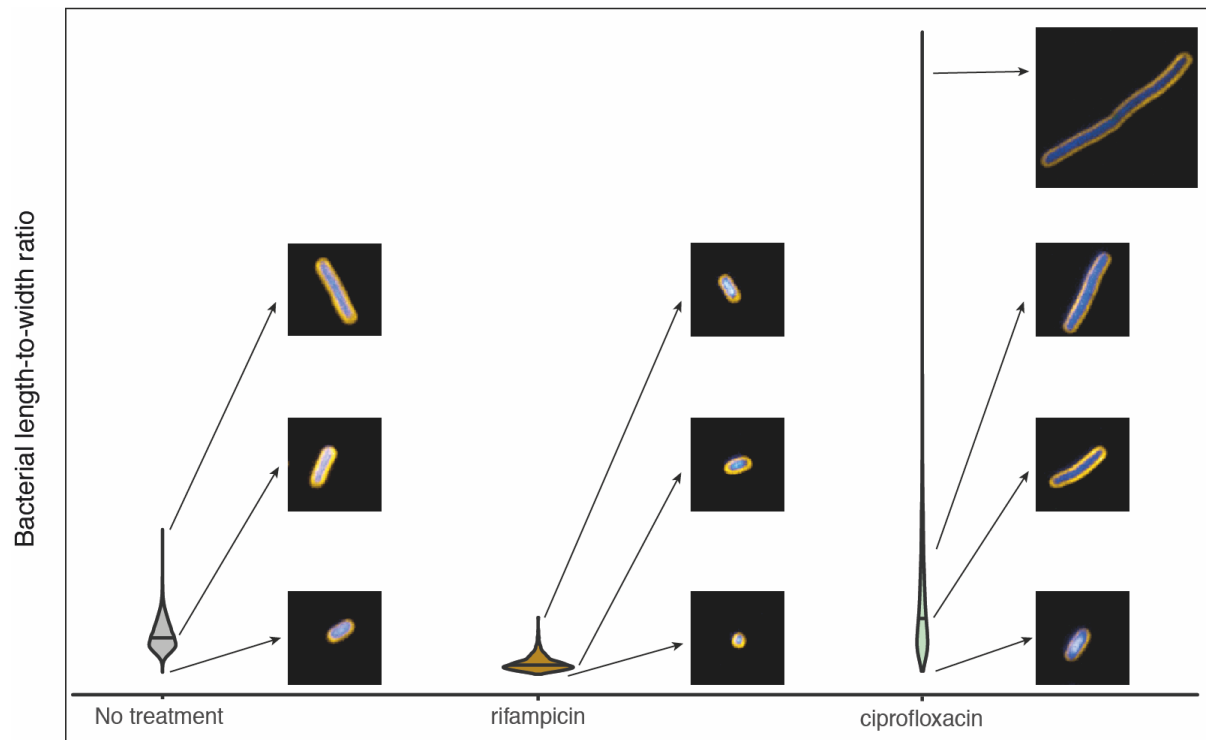
619 comparing *K. pneumoniae* NCTC 43816 and *S. Typhimurium* NCTC 13348 treated with

620 meropenem, cefturoxime, rifampicin, tigecycline and ciprofloxacin, and *S. aureus*

621 ATCC29213 treated with ciprofloxacin, vancomycin, gentamicin and oxacillin, with

622 untreated controls.

623



624

625 **Figure 8: Example of population-level length heterogeneity of *K. pneumoniae* NCTC**

626 **43816.** Violin plot of bacterial length-to-width ratio comparing untreated, rifampicin treated,

627 and ciprofloxacin treated *K. pneumoniae* NCTC 43816 with inset images demonstrating the

628 different phenotypes observed in the same growth conditions within a single well.

629